JGR Atmospheres

RESEARCH ARTICLE
10.1029/2023JD038693

Special Section:
Atmospheric Rivers: Intersection of Weather and Climate

Large-Scale Circulation Context for North American West Coast Atmospheric Rivers: Influence of the Subseasonal NPO/WP Teleconnection

Justin Hicks[1], Bin Guan[2,3], Sumant Nigam[1], and Alfredo Ruiz-Barradas[1]

[1]Department of Atmospheric and Oceanic Science, University of Maryland, College Park, College Park, MD, USA, [2]Joint Institute for Regional Earth System Science and Engineering, University of California, Los Angeles, Los Angeles, CA, USA, [3]Jet Propulsion Laboratory, California Institute of Technology, Pasadena, CA, USA

Abstract Understanding the variability of atmospheric rivers (ARs) on subseasonal time scales is pivotal for efficient water resource management along the west coast of North America. ARs during 1980–2018 based on the Modern-Era Retrospective analysis for Research and Applications, version 2 are analyzed to quantify the modulation of winter (December–February) landfalling ARs in the western US by leading subseasonal teleconnections, focusing on pentad evolution rather than seasonal-mean patterns. The growth phase of the North Pacific Oscillation/West Pacific (NPO/WP) teleconnection—the second leading pattern in 200-hPa geopotential heights in boreal winter—is found to be particularly influential in modulating the number of landfalling ARs in this region. In the positive phase of NPO/WP growth, the presence of anomalous low pressure centered just south of Alaska (i.e., a strengthening of the Aleutian Low) and anomalous high pressure around Hawaii results in moisture convergence in the central and eastern Pacific, bringing southwesterly moisture fluxes to the coast and inland. The modulation by NPO/WP is stronger than by commonly-considered climate variability modes, such as the Pacific/North American (PNA) pattern. Although southwesterly fluxes are stronger over the Pacific Ocean during the positive phase of PNA, they tend to transition to southerly fluxes before extending inland, resulting in smaller overland impacts in the western US. The analysis of temporal evolutions indicates AR activity peaks 5 days after the mature phase of NPO/WP growth, as in the case of PNA. Overall, the study suggests potential subseasonal predictability of US West Coast ARs from incipient-phase knowledge of the leading teleconnection patterns, especially the NPO/WP.

Plain Language Summary Atmospheric rivers (ARs) are "rivers in the sky" that transport vast amounts of water vapor—equivalent to about 27 Mississippi Rivers on average for those observed in the northeastern Pacific. As major precipitation deliverers, flood producers, and drought busters, ARs represent a key meteorological phenomenon of societal importance in the semi-arid western US. Understanding how large-scale climate conditions, such as El Niño and La Niña, influence the occurrence and strength of ARs is pivotal for efficient water resource management in the region. Of particular interest to water managers are AR activity variations on the subseasonal-to-seasonal time scales, that is, on time scales beyond the typical 1–2-week period of weather forecasts. Focusing on these time scales, the current study identifies a subseasonal weather pattern that is particularly influential on AR activity in the western US. The North Pacific Oscillation/West Pacific teleconnection pattern (NPO/WP) is more influential than other subseasonal patterns previously linked to AR activity, both in terms of landfall occurrence and inland reach. Our findings advance prospects of subseasonal prediction of winter AR activity over the western US, from the incipient-phase knowledge of the impactful subseasonal teleconnections operating over the Pacific-North American region, especially the NPO/WP.

Key Points:

- The modulation of atmospheric rivers (ARs) in the western US by climate variability modes is analyzed, focusing on pentad evolution
- The North Pacific Oscillation/West Pacific (NPO/WP) pattern is more influential on western US AR activity than commonly-considered modes
- The finding advances prospects of subseasonal prediction of ARs over the western US from the NPO/WP's incipient-phase knowledge

Correspondence to:
B. Guan,
bin.guan@jpl.nasa.gov

Citation:
Hicks, J., Guan, B., Nigam, S., & Ruiz-Barradas, A. (2023). Large-scale circulation context for North American west coast atmospheric rivers: Influence of the subseasonal NPO/WP teleconnection. *Journal of Geophysical Research: Atmospheres*, *128*, e2023JD038693. https://doi.org/10.1029/2023JD038693

Received 10 FEB 2023
Accepted 26 JUL 2023

1. Introduction

Of particular importance to societies around the world are the availability of water and the occurrence of extreme hydroclimatic events like floods and droughts. Prediction of weather-related hydrometeorological events requires not only an understanding of the atmospheric and background ocean-related climatic conditions—for instance, Pacific and Atlantic decadal variability and El Niño/Southern Oscillation (ENSO)—but also of the hydrologic processes particular to a given basin. A key link between the local hydrometeorological events and the global-scale phenomena that may be forcing them is the transport of moisture (or the lack of it). In this research, attention will be paid to this mentioned link, by focusing on the analysis of atmospheric rivers (ARs) and their modulation by

global climate phenomena at subseasonal scales—a time scale of key importance to the management of water resources, droughts, and floods.

1.1. Atmospheric Rivers and Their Impacts

The term "atmospheric river" (AR) was coined by Zhu and Newell (1994) to refer to long and narrow filaments of enhanced water vapor transport in the lower troposphere. These transient synoptic features, in some cases related to the concepts of "moist tongue" and "warm conveyor belt" (Mo, 2022), are responsible for over 90% of the poleward transport of water vapor across the midlatitudes, despite covering only ∼10% of the Earth's area in the midlatitudes (Zhu & Newell, 1998). Although ARs can occur in the warm season (e.g., Mo et al., 2022), they are typically prevalent in the winter months in the western US, when the air is more saturated, vapor fluxes are stronger, and vertical motion is enhanced (Neiman et al., 2008). ARs are responsible for high-impact flooding events in many regions of the world, such as the western US (Bao et al., 2006; Guan et al., 2013; J. Kim et al., 2018; Neiman et al., 2008; Ralph et al., 2006; Tan et al., 2022; among many others), the central US (Lavers & Villarini, 2013b), western Europe (Lavers et al., 2012; Lavers & Villarini, 2013a), and Canada (Mo et al., 2019; Sharma & Déry, 2020; Smirnov & Moore, 1999). Despite the monetary costs of these immense precipitation events, such as contributing to nearly 90% of flood-related insured losses in the western US (Corringham et al., 2019; Prince et al., 2021), ARs are responsible for bringing a large fraction of precipitation to drought-prone areas, often breaking existing drought conditions (Dettinger, 2013). For example, the western US receives 30%–50% of the winter precipitation from AR events (Dettinger et al., 2011; Guan et al., 2010; J. Kim et al., 2018; Rutz & Steenburgh, 2012)—a result also found in many other regions. The broad spectrum of potential AR impacts, from being mostly beneficial to mostly hazardous, is reflected in the recently introduced AR scale (Eiras-Barca et al., 2021; Guan et al., 2023; Ralph et al., 2019). Previous studies have noted the variability of ARs on a variety of time scales, from subseasonal to interannual, with implications on their predictability and predictions. Therefore, it is important that we understand not only the seasonality of the ARs impacting a given region but also the way they can be modulated in time and space from large-scale climate phenomena via teleconnections.

1.2. Atmospheric Teleconnections

Global phenomena like the Pacific and Atlantic decadal variability and ENSO modify the climatological precipitation and temperature around the world by establishing connections between remote regions (e.g., Baxter & Nigam, 2015). The temporal scale of these patterns varies from a period of days to decades. Previous studies have correlated certain teleconnections with the frequency and intensity of ARs across multiple regions. For example, Bao et al. (2006), Dettinger (2004), and Guan et al. (2013) compared the intensity and frequency of ARs in the western US to the phase of ENSO, which is responsible for the fluctuation in sea surface temperatures and sea level pressure (SLP) across the equatorial Pacific. Other studies have examined the relationship between AR frequency in the western US and ENSO diversity, particularly the El Niño Modoki (H.-M. Kim et al., 2019; Weng et al., 2009). Compared to ENSO, the Pacific-Japan teleconnection pattern and East Asian subtropical jet were found to be more influential to interannual variability of western US ARs (Zhang & Villarini, 2018). The modulation of AR activity in the northeastern Pacific and western US by the Madden Julian Oscillation, a leading component of tropical intraseasonal variability, has been examined in a number of studies (e.g., Guan et al., 2012; Guan & Waliser, 2015; Mundhenk et al., 2016; Wang et al., 2023; Zhou et al., 2021). Other studies have focused on subseasonal teleconnection patterns that have a more direct extratropical expression. For example, the Pacific/North American (PNA) pattern, a quadruple structure of 500-hPa geopotential height anomalies in the Pacific-North American region, has been found to influence AR frequency and AR-related snow accumulation in the western US (Guan et al., 2013; Guan & Waliser, 2015). The Arctic Oscillation (AO), characterized by SLP anomalies of one sign in the Arctic and of the opposite sign in the extratropics, is another teleconnection that has been linked to AR activity in the western US (Guan et al., 2013; Guan & Waliser, 2015). There are similar studies that quantified the relationship between teleconnections and AR events outside of the western US. For example, Lavers and Villarini (2013a) explored the connection between AR frequency in northern/southern Europe and the North Atlantic Oscillation (NAO), a regional expression of the AO. Lavers and Villarini (2013b) also explored the effects of the NAO on AR-related flooding in the central US. Strong modulation of AR activity in western Europe by the stratospheric polar vortex is recently noted (Lee et al., 2022). Unlike most of the

other well established large-scale modes of climate variability, the relationship between ARs and the North Pacific Oscillation/West Pacific (NPO/WP) teleconnection has only been noted in Brands et al. (2017), Guirguis et al. (2019), and Tan et al. (2020). The NPO/WP pattern is characterized by a large-scale meridional dipole in SLP and geopotential height over the Pacific, and is linked to meridional movements of the Asian-Pacific jet and variability of the Pacific storm track (Linkin & Nigam, 2008). The Guirguis et al. (2019) study, which focused on northern California, highlighted the more influential role of certain subseasonal modes (including WP), compared to ENSO, in modulating AR activity in California.

With a special focus on the NPO/WP pattern, the objective of this research is to investigate the influence of the variability in subseasonal winter circulations (teleconnections) on the spatial and temporal distribution of ARs in the western US. This research will take advantage of an AR database that has been widely used and evaluated. Assessing the predictability of ARs from these results could help regions prone to AR events manage their water resources more effectively.

2. Data and Methods

2.1. Rotated Extended EOF Analysis

An extended and rotated empirical orthogonal function (EOF) analysis was used to extract the leading modes of subseasonal variability. The EOF analysis determines the structure of recurrent variability, including the spatial patterns and the extent to which they are present; these recurrent patterns are known as teleconnection patterns when they connect regions far apart from one another (Nigam, 2003). A correlation or covariance matrix is typically used for this analysis—each row of the matrix represents separate maps for a single time step and each column represents a time series for a single location. The next step requires finding the eigenvectors of the correlation/covariance matrix corresponding to its eigenvalues. The eigenvector gives the spatial pattern of the EOF, and the eigenvalue (when divided by the sum of all eigenvalues) gives the fraction of the total variability explained by the EOF (Björnsson & Venegas, 1997). In extended EOF, the spatial pattern and temporal evolution of a variability mode are accounted for simultaneously, facilitating the extraction of non-stationary, propagating modes (Weare & Nasstrom, 1982). In order to simplify the structure and easily interpret the patterns in the EOFs, a rotation matrix is applied to the leading EOFs, and the result is a number of localized modes that are dependent on the number of EOFs retained (Hannachi, 2004).

2.2. Analyzed Teleconnection Patterns

Using the above method, the principal components are computed for 200-hPa geopotential height anomalies from the NCEP/NCAR reanalysis (Kalnay et al., 1996) on the Northern Hemisphere domain at 2.5° × 2.5° spatial resolution and at pentad (5-day averages) temporal resolution for the extended winter covering from November to March for the period 1979–2019. A five-pentad lead/lag sequence, combined in the way described in Weare and Nasstrom (1982), is used for the extended EOF analysis, with the five leading modes rotated. Although teleconnection analyses are often conducted using data at the 500-hPa level, it is expected that an EOF analysis at the 200-hPa level facilitates the extraction of modes with potential interactions between the tropics and the midlatitudes (Baxter & Nigam, 2013). The five leading variability patterns in order of explained variance include the NAO, NPO/WP growth, NPO/WP decay, the PNA, and the Scandinavian (SCAND) pattern, as described in Baxter and Nigam (2013, 2015). The designation of the growth versus decay phase of NPO/WP is based on the evolution of the spatial patterns over the five-pentad sequence from the extended EOF. Their corresponding principal components are shown in Figure 1 (left column) along with their spatial distribution of 850-hPa geopotential height anomalies (right column).

2.3. AR Database

In this study, a historical AR database (Guan et al., 2018; Guan & Waliser, 2015) is used. The shapes of each AR event are cataloged every 6 hr for the period of 1980–2018 and were computed on a 0.5° × 0.625° global grid. Each AR is defined by the integrated vapor transport (IVT) intensity, direction, and geometry, each of which was computed using the Modern-Era Retrospective analysis for Research and Applications, version 2 (MERRA-2) reanalysis (Gelaro et al., 2017). IVT is calculated as

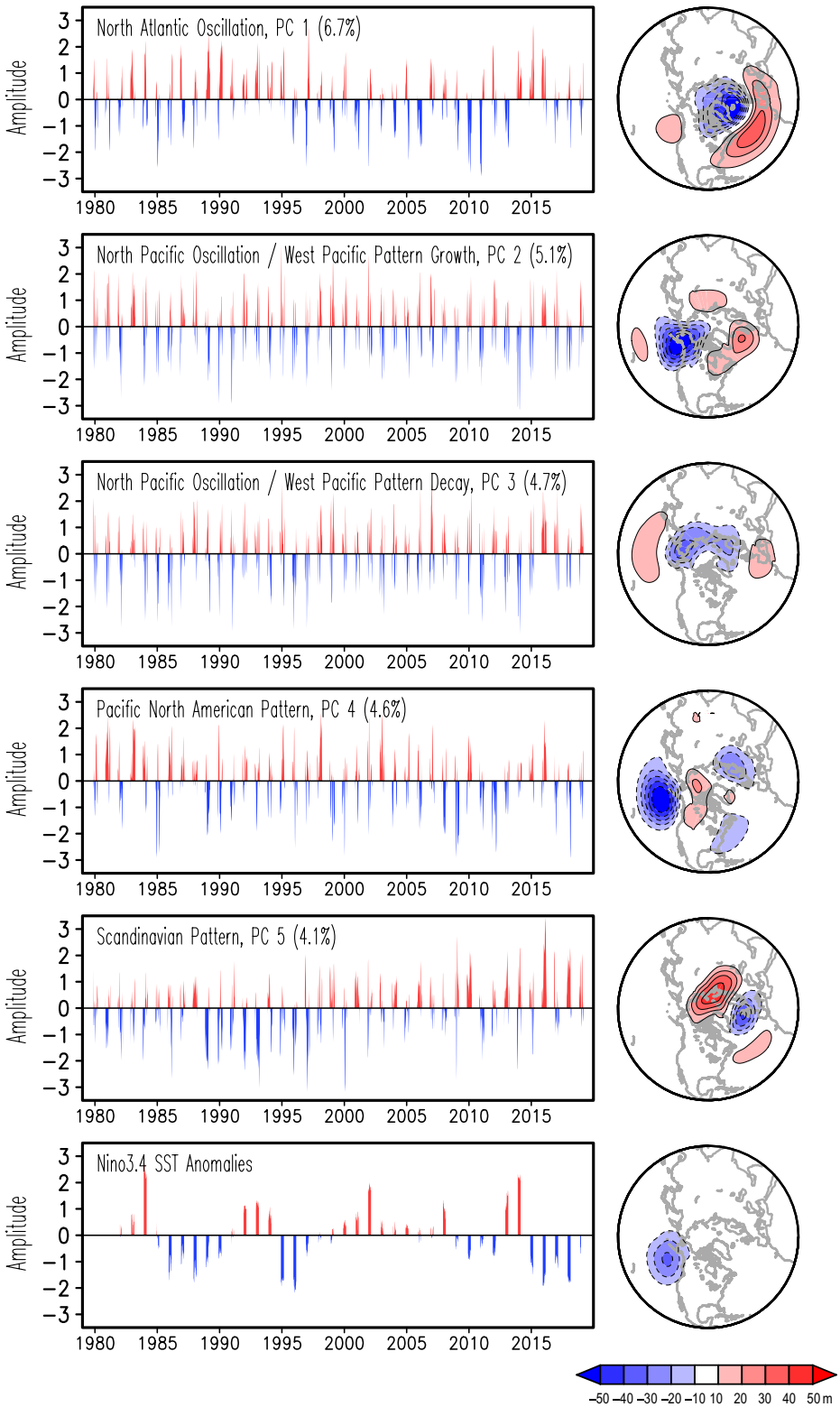

Figure 1.

$$\sqrt{\left(\frac{1}{g}\int_{p_0}^{p_1} q \cdot u \cdot dp\right)^2 + \left(\frac{1}{g}\int_{p_0}^{p_1} q \cdot v \cdot dp\right)^2} \quad (1)$$

where g is the acceleration due to gravity (m/s^2), p_0 is the surface pressure, p_1 is 300-hPa, q is the specific humidity (kg/kg), dp is the difference in pressure between the top and bottom of each atmospheric layer, and u/v are the zonal/meridional velocity components of wind, respectively. As described in Guan and Waliser (2015), ARs included in this database are at least 2,000 km long with a length/width ratio of at least 2:1, have a notable mean poleward IVT (>50 kg m^{-1} s^{-1}), and have IVT at all individual grid cells above the threshold of 100 kg m^{-1} s^{-1}, or the season-and-location-dependent 85th percentile—whichever is larger. This global AR database has been compared to selected regional AR catalogs in western North America, Britain, and East Antarctica that were independently created by other studies using different techniques, and shows over 90% agreement with them in terms of AR landfall dates (Guan & Waliser, 2015). This database has been formally evaluated against dropsonde observations in terms of basic AR characteristics such as width and total IVT across the width, and thus has often been used as a benchmark in other studies (e.g., Eiras-Barca et al., 2018; Lakshmi et al., 2019; Yang et al., 2018). It is noted that AR characteristics may be sensitive to the AR detection method used (Collow et al., 2022; O'Brien et al., 2022; Rutz et al., 2019; Shields et al., 2018, 2023), and AR detection methods could be sensitive to the input data product, including its resolution. The detection method used in the current AR database is found to be particularly robust to the input data (Collow et al., 2022, their Figures 3 and 4), as will also be illustrated here. A better understanding of the different AR detection methods is needed to help reconcile their discrepancies and improve the accuracy of AR detection.

2.4. AR Frequency and Other Pentad-Resolved Anomalies

Each grid point that contained an AR in any given 6-hourly timestep was substituted with a value of 1; conversely, grid points without an AR present were filled with a value of 0. The entire data set was then re-binned from 6-hourly time steps to pentads by summing up the binary AR tags over each 5-day period, creating a data set of pentad AR frequency. For example, a pentad with an AR that lasted 24 hr (i.e., four 6-hourly time steps) would have an AR frequency of 4. To have a consistent number of pentads per year (73 pentads = 1 year), leap days were omitted from the catalog by constraining the data set to a 365-day calendar. A climatology was constructed for each pentad by averaging corresponding pentads from the years 1980–2018. Anomalies were then computed by subtracting the climatological average from each individual pentad. Pentad resolved anomalies of 850-hPa geopotential heights from MERRA-2, horizontal/meridional winds from the NCEP/NCAR reanalysis, and observed precipitation from NOAA's Climate Prediction Center were also constructed. Finally, a Niño 3.4 sea surface temperature (SST) index was constructed from daily winter NOAA Optimum Interpolation (OI) SST anomalies from 1982 to 2018 within the area bounded by 120°–170°W and 5°S–5°N.

2.5. Contemporaneous and Lead/Lag Regression Analysis

Teleconnection patterns and their modulation of ARs are analyzed in extended winter months (NDJFM) when ARs are most active along the west coast of North America, impacting areas from Mexico to southern Alaska (e.g., contour lines in Figure 2). The variability of ARs increases from November to January along the coastal US and the central to north Pacific basin and decreases thereafter (e.g., shadings in Figure 2). The analysis is thus constrained to only boreal winter. The winter AR anomalies were linearly regressed onto the five leading principal components (teleconnection patterns) of the Northern Hemisphere circulation described above to explore their influence on AR variability. The evolution of AR anomalies (i.e., their spatiotemporal variability) was constructed using lead/lag regressions. This procedure demonstrates the behavior of the AR anomalies preceding and following the contemporaneous (mature) phase of each teleconnection pattern. The results were then assessed and the teleconnections with the most significant influence on landfalling ARs were identified.

Figure 1. The five leading subseasonal principal components (left) and related spatial patterns (regressions of 850-hPa geopotential height; right) from an extended rotated-EOF analysis of 200-hPa geopotential heights (from NCEP/NCAR reanalysis) at pentad resolution in extended winter (November–March) during 1979–2019. From the top: the North Atlantic Oscillation (NAO), the growth phase of North Pacific Oscillation/West Pacific (NPO/WP) pattern, the decay phase of NPO/WP, the Pacific North American (PNA) pattern, and the Scandinavian (SCAND) pattern. The ENSO teleconnection, from regressions on the Niño 3.4 sea surface temperature (SST) index during 1982–2018, is at the bottom. The explained variance is noted next to the teleconnection name. Red/blue represent positive/negative height anomalies, with contour lines drawn every 10 m and the zero-contour suppressed.

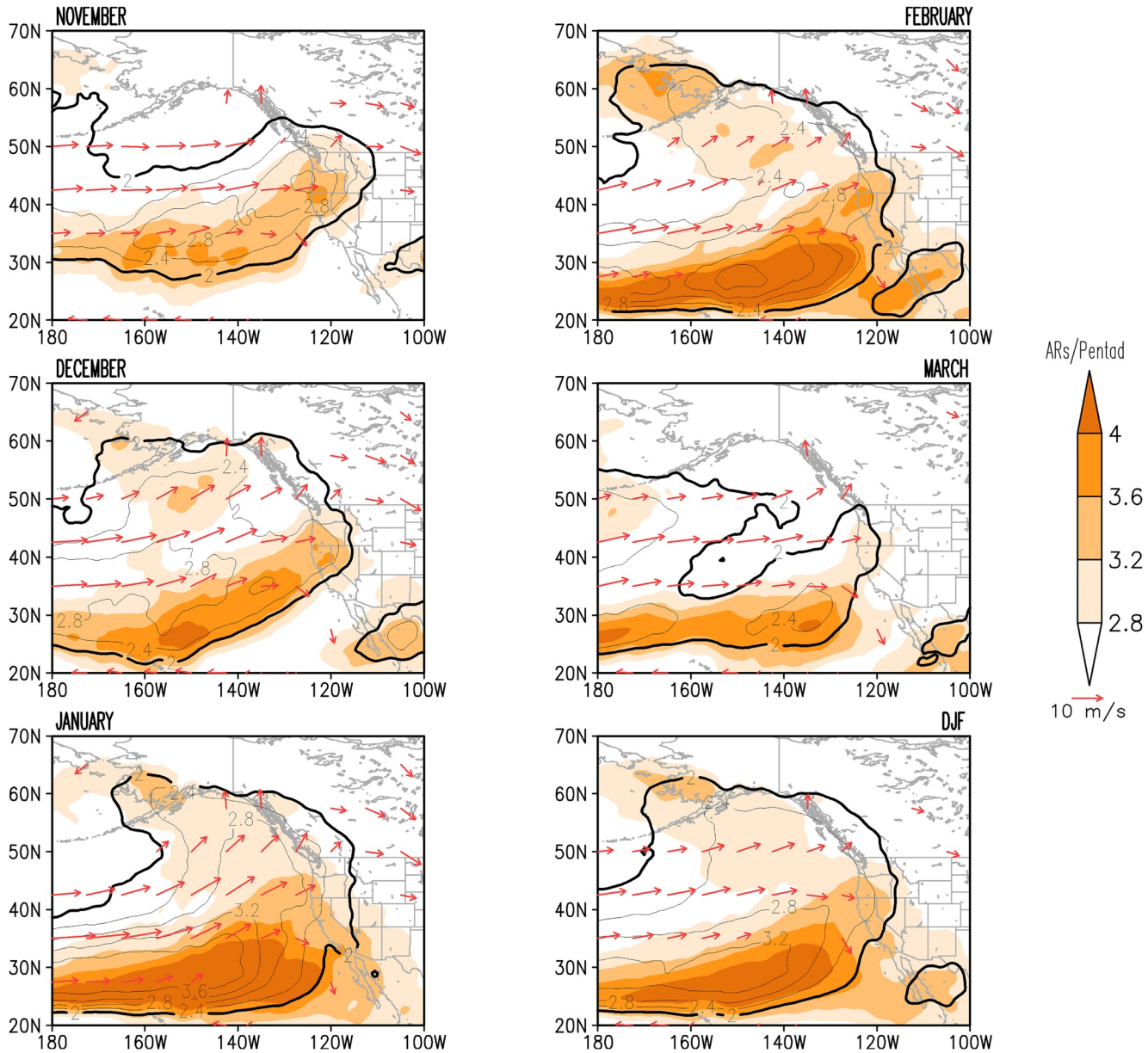

Figure 2. Monthly standard deviation and climatology of atmospheric river (AR) counts from NASA's Modern-Era Retrospective analysis for Research and Applications, version 2 (MERRA-2) 1980–2018 pentad-resolution atmospheric reanalysis. Standard deviation is shaded in orange (see color bar) and the climatology contoured in black with the 2 ARs/pentad isoline thickened for emphasis. Climatological 850-hPa winds are shown with red vectors when larger than 4 m/s. A 9-point spatial smoother is applied once to the standard deviation and AR climatology. Note that in this figure and subsequent figures, the AR frequency unit, ARs/pentad, indicates the number of 6-hourly time steps per pentad during which AR conditions are present (a given AR event may last multiple 6-hourly time steps and is counted so).

Of interest here is practical significance (Kirk, 1996), rather than statistical significance, which, in the current study, is assessed based on identifying mode(s) with influences larger than those associated with better-studied modes. The 850-hPa geopotential heights and observed precipitation were also regressed onto each of the tele-connection patterns to analyze the dynamics that modulate moisture fluxes and compare anomalously wet and dry regions with those that experience anomalous AR activity, respectively. A similar analysis based on the Niño 3.4 index is also included. Although ENSO is considered an interannual pattern of variability, it is able to influence subseasonal AR variability, and provides a baseline for assessing the strengths of the modulation by the leading circulation patterns.

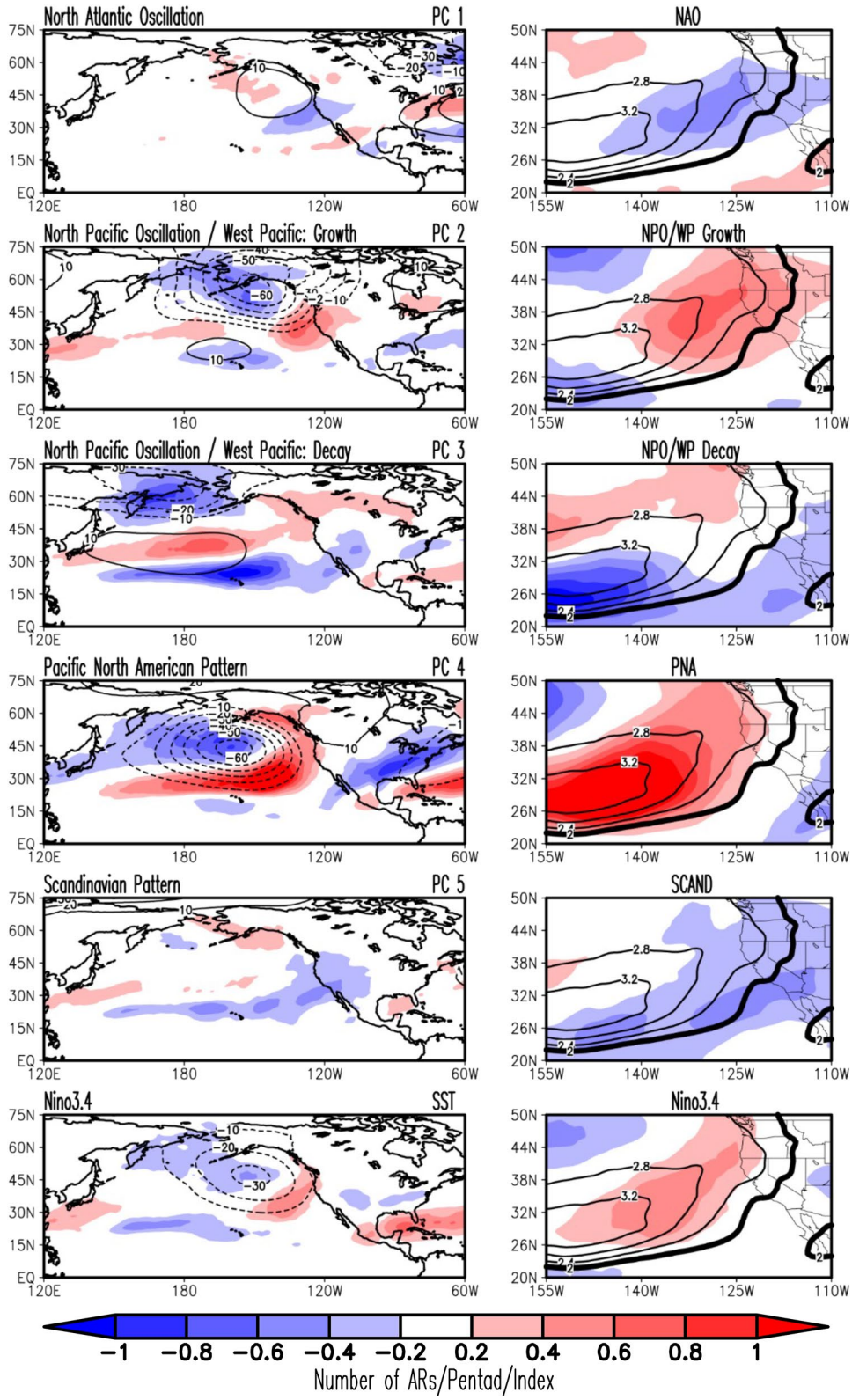

Figure 3.

3. Results

The influence of the leading circulation patterns and ENSO on AR activity along coastal areas in the western US is shown in Figure 3 by the linear regressions of MERRA-2 AR frequency anomalies on the time series of these variability patterns (see Figure 1). A comparison between results using MERRA-2 and ERA-Interim ARs (Figure 4) reveals nearly identical patterns of climatological AR frequency and its modulation by the leading circulation patterns, except the patterns based on ERA-Interim are smoother due to the coarser horizontal resolution. Therefore, only MERRA-2 is used in subsequent analysis. The discussion below focuses on NPO/WP (both growth and decay phases) and PNA whose influences on AR activity are the most prominent, and ENSO which provides a baseline for comparison. Two other patterns—the NAO and the SCAND patterns, are not analyzed in detail due to their less prominent influence on ARs along the west coast of the US.

3.1. Niño 3.4 Regression

SSTs within the Niño 3.4 region correlate with SLP and geopotential height anomalies in the North Pacific, the latter of which are shown in the bottom-left of Figure 3 (simultaneous regression over a Pan-Pacific domain) and the last column of Figure 5 (lead/lag regressions over the northeastern Pacific). Because interannual El Niño events are not as transient as subseasonal patterns of variability, there is little evolution in the spatial variability of 850-hPa geopotential height anomalies 2 pentads before (denoted "$t - 2$" in Figure 5) the mature (denoted "t") phase of El Niño and 2 pentads after ("$t + 2$") the mature phase. Areas shaded in red exhibit higher AR frequencies and areas shaded in blue experience less frequent AR frequencies during El Niño (positive phase of ENSO) conditions relative to the pentad-resolved climatology. The regressions show an anomalous area of below-average 850-hPa geopotential heights (~30 m less than the climatological average) in the Gulf of Alaska, centered around 45°N and 150°W. The lower pressure brings anomalous southerly/southwesterly winds to the west coast of the US and the Pacific Northwest.

The red shading in the bottom-right of Figure 3 (simultaneous regression) and the last column of Figure 6 (lead/lag regressions) shows the resulting anomalous AR frequency, where an increase in AR frequency originates northeast of Hawaii and downstream of the lower 850-hPa geopotential heights discussed above. There is only a small and marginal influence on landfalling ARs in western North America during El Niño events, as the lower-tropospheric circulation anomaly driving moisture transport is generally parallel to the coastline (see Figure 5). The AR frequency doesn't surpass 0.4 AR/pentad and is constrained mostly to coastal areas in Oregon and northern California. This is consistent with the general precipitation pattern in the last column of Figure 7. Relative to the winter climatology, ARs during El Niño events propagate further east (comparing the black contours and color shading in Figure 3, bottom right). In the La Niña phase, a decrease in AR landfall frequency would arise on the west coast, resulting from an increase in 850-hPa geopotential heights in the Gulf of Alaska and a decrease in moisture fluxes toward the coast.

3.2. NPO/WP Regression

Nigam (2003) summarizes the NPO/WP pattern as exhibiting anomalous heights and SLP over the Bering Strait, extending equatorward along the west coast of the US; a second area of variability of opposite signs extends from the Korean peninsula to Hawaii. This can be seen in the second and third panels in Figure 3 left (simultaneous regressions over a Pan-Pacific domain) and the second and third columns of Figure 5 (lead/lag regressions over the northeastern Pacific), where anomalously low 850-hPa heights are situated over the Aleutian Islands (extending from east Asia to central Canada) and anomalously high heights extend from Hawaii toward east Asia. In this case, lower heights poleward of 30°N represent a developing positive phase of the NPO/WP (Figure 5, second column). The anomalous low heights have a much greater magnitude (<−50 m) than the anomalous high heights (~20 m) per index value, consistent with the description of the teleconnection pattern in Nigam (2003). From $t - 2$ to $t + 2$, the evolution of both dipoles can be seen.

Figure 3. *Left Panels*: Characteristic *pentad* atmospheric river (AR) counts and 850-hPa height anomalies associated with the leading subseasonal teleconnection patterns and El Niño variability from Niño3.4 sea surface temperature (SST) index during the extended winter season (November–March), obtained from linear regressions during 1980–2018 and 1982–2018, respectively. From top to bottom: the North Atlantic Oscillation (NAO), the growth phase of North Pacific Oscillation/West Pacific (NPO/WP) pattern, the decay phase of NPO/WP, the Pacific North American (PNA) pattern, the Scandinavian (SCAND) pattern, and El Niño. Positive/negative AR regressions are shaded red/blue at 0.2 AR/pentad interval; 850-hPa height anomalies are contoured at 10 m interval with continuous/dashed lines for positive/negative anomalies. *Right Panels*: AR regressions are superposed on the AR climatology in the Pacific–North American region, where climatological AR counts are contoured at 0.4 AR/pentad; the 2.0 ARs/pentad anomaly contour is thickened for emphasis. A 9-point spatial smoother is applied twice to the AR regressions and climatology.

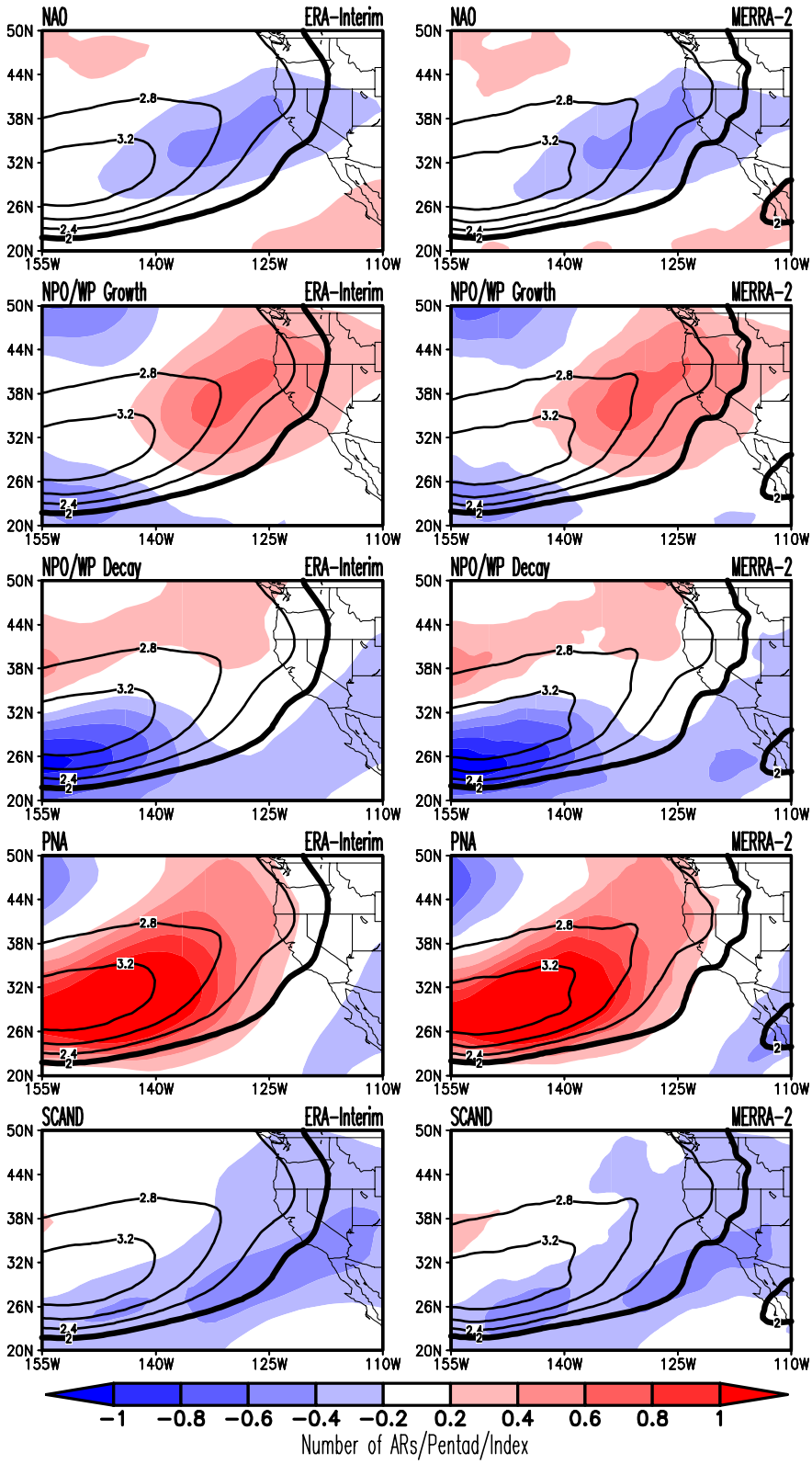

Figure 4.

From $t-1$ to the mature phase (t) of the developing positive NPO/WP, there is a significant increase in the gradient of the anomalously high 850-hPa heights (Figure 5, second column) and the 850-hPa heights themselves (not shown). This is indicative of an increase in the moisture flux toward the west coast of North America via a southwesterly flow. This area develops into a region of enhanced moisture transport, contributing to anomalously high frequency of ARs (Figure 6, second column). In this leading pattern of variability, the AR anomalies over the northeastern Pacific and along the west coast of the US are greater than those of ENSO. Under a developing positive NPO/WP, some regions in the Pacific Northwest have twice the AR frequency anomaly (~0.8 AR/pentad) relative to under El Niño conditions. As the higher geopotential heights develop and begin to extend out from the vicinity of Hawaii (i.e., from t to $t+1$ in Figure 5, second column), an area of less frequent AR activity can be seen near Baja California (i.e., from $t+1$ to $t+2$ in Figure 6, second column) due to anomalous easterlies across the Baja Peninsula and northern Mexico resulting from the high anomaly. The decay phase of the positive NPO/WP, as shown in the third column of Figure 5, has a similar dipole in geopotential heights, but lags the growth phase by about 10 days. Regression of both NPO/WP phases onto precipitation indicates coastal communities along the west coast of North America—from northern California to British Columbia—tend to receive more precipitation around the maturing stage of positive NPO/WP (t for the growth phase and $t-2$ for the decay phase; second and third columns in Figure 7), and that the influence of NPO/WP on precipitation is stronger and more extensive than previously described for ENSO. Although AR frequency and precipitation anomalies peak at slightly different lags, the overall northward progression of precipitation anomalies along the west coast of North America associated with NPO/WP is consistent with the northward progression of AR frequency anomalies along the coastal areas. For example, for NPO/WP growth, precipitation anomalies are most coherent between Washington and California at $t-1$, which extend to coastal western Canada at t, and further extend to southern Alaska but retreat northward in California at $t+1$. The corresponding AR anomalies extend from between Washington and California at t to western Canada at $t+1$, and to southern Alaska at $t+1$. Relative to the winter climatology, ARs during the positive phase of NPO/WP growth shift the tract northeast, allowing for greater coastal influence (comparing the black contours and color shading in the second panel of Figure 3 right).

3.3. PNA Regression

The positive PNA pattern can be seen in the fourth panel of Figure 3 left and the fourth column of Figure 5. Negative 850-hPa geopotential heights anomalies can be seen extending zonally from East Asia to the coast of the western US and meridionally from the Bering Strait to the vicinity of Hawaii. Positive 850-hPa geopotential height anomalies are seen in central/western Canada and extend poleward. This displacement in geopotential height anomalies is consistent with those shown in Baxter and Nigam (2013). The geopotential height anomalies centered in the north-central Pacific have a much greater magnitude than those to its northeast. The strongest geopotential height anomaly is less than −50 m from $t-2$ to $t+1$, comparable to the anomaly seen in the North Pacific in the NPO/WP analysis, except with a more southward position.

From $t-2$ to the mature phase (t), an increasing geopotential height gradient is present, indicative of an increase in southwesterly moisture fluxes toward the west coast. Consequently, there is a greater AR frequency during the positive phase of the PNA north of northern California (fourth column of Figure 6). The landfalling AR frequency anomaly is only slightly positive (maximum of ~0.4 AR/pentad) because the moisture fluxes run nearly parallel to the coastline, indicating limited moisture convergence along the west coast of the US. Southerly moisture fluxes instead bring the majority of this moisture to southeastern Alaska, British Columbia, and the southwestern portion of the Yukon territory. However, the magnitude of the offshore anomalies over the northeastern Pacific Ocean (>1 AR/pentad) is greater than those of the NPO/WP pattern, attributable to the more southward (i.e., closer to the tropical moisture reservoir) location of the circulation anomaly center. As the moisture approaches the coast, the southerly component of the fluxes dominates. Associated with the marginal positive AR frequency

Figure 4. Inter-reanalysis comparison of climatological atmospheric river (AR) counts and AR-count regressions on winter teleconnections during 1980–2018: Modern-Era Retrospective analysis for Research and Applications, version 2 (MERRA-2) (right column) and ERA-Interim (left column). From the top: regressions on the North Atlantic Oscillation (NAO), the growth phase of North Pacific Oscillation/West Pacific (NPO/WP) pattern, the decay phase of NPO/WP, the Pacific North American (PNA) pattern, and the Scandinavian (SCAND) pattern. AR regressions are shaded red/blue for positive/negative values at 0.2 AR/pentad/index interval (see color bar). The climatological AR count per pentad is contoured in black at 0.4 intervals, with the 2.0 ARs/pentad isoline thickened for emphasis. A 9-point spatial smoother is applied twice to AR regressions and climatology.

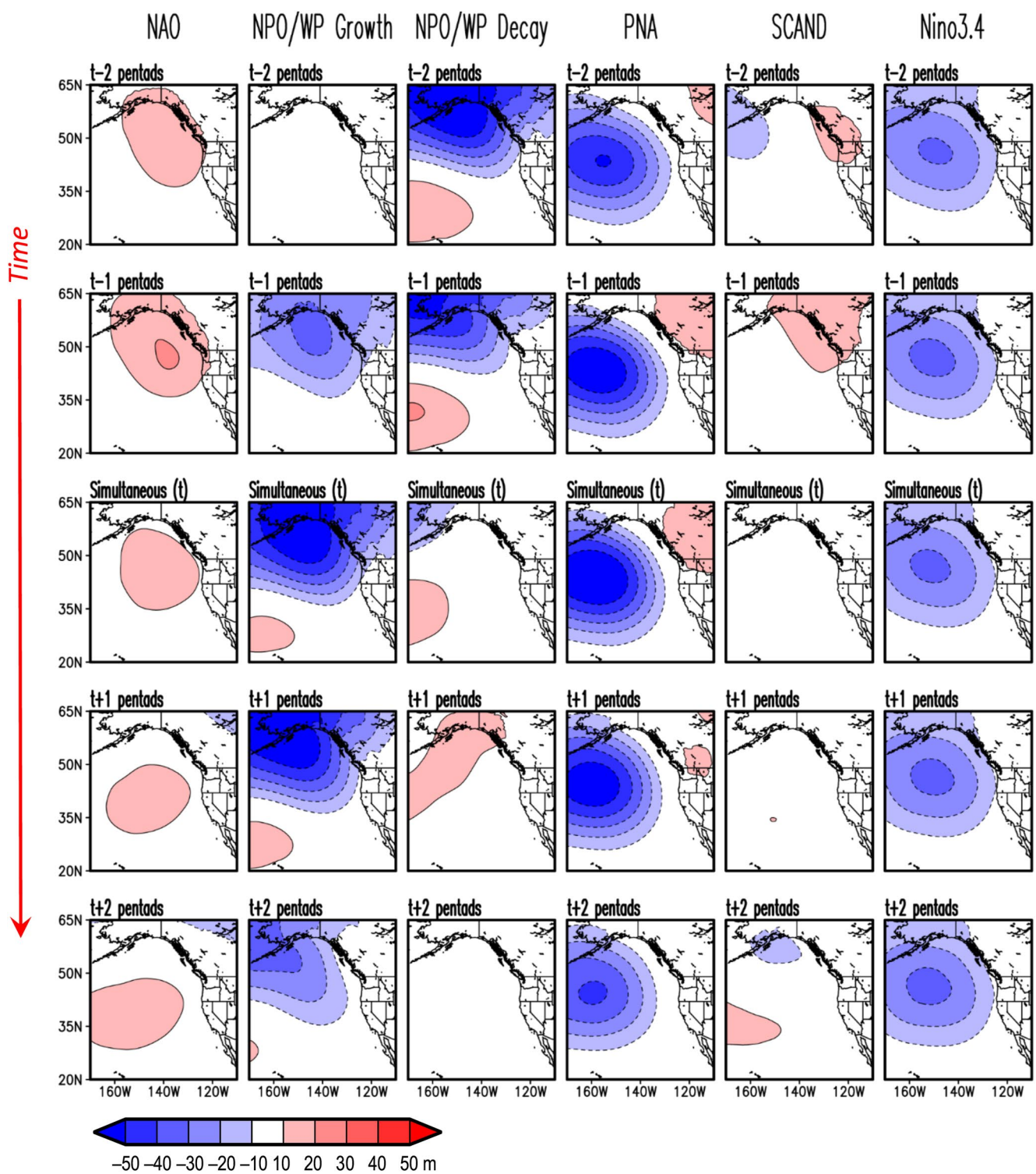

Figure 5. *Pentad* evolution of 850-hPa geopotential heights associated with leading subseasonal winter teleconnections and El Niño variability along the North American West Coast. Time runs downward from $t - 2$ to $t + 2$ pentads. Anomalies are obtained from *pentad* lead-lag regressions of height on the circulation principal components and the Niño 3.4 sea surface temperature (SST) index. From left: the North Atlantic Oscillation (NAO), the growth phase of North Pacific Oscillation/West Pacific (NPO/WP) pattern, the decay phase of NPO/WP, the Pacific North American (PNA) pattern, the Scandinavian (SCAND) pattern, and El Niño. Height regressions are shaded red/blue for positive/negative anomalies at 10 m/index intervals with the zero-contour suppressed.

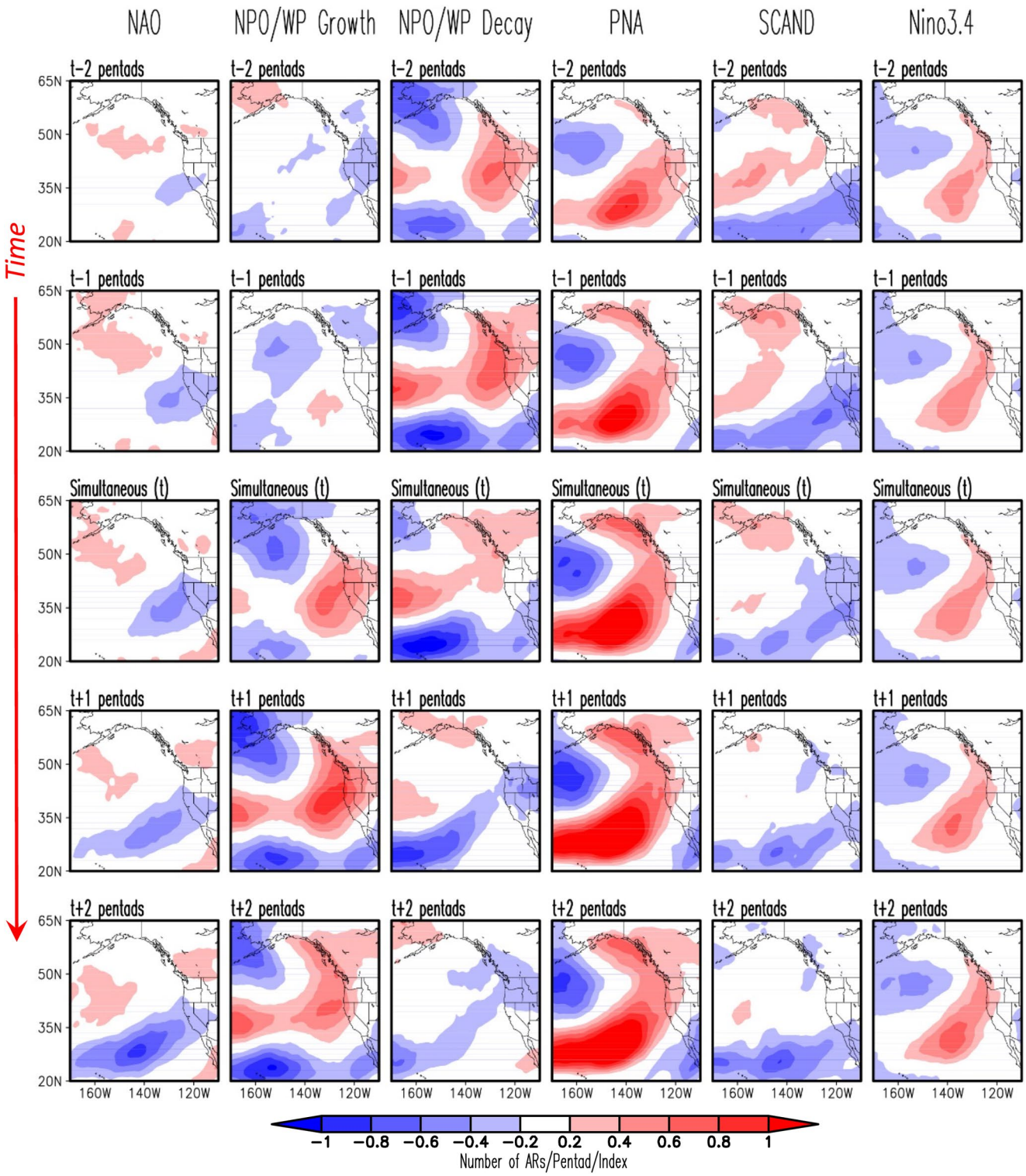

Figure 6. *Pentad* evolution of atmospheric river (AR) counts associated with leading subseasonal winter teleconnections and El Niño variability along the North American West Coast. Time runs downward from $t-2$ to $t+2$ pentads. The anomalies are obtained from *pentad* lead-lag linear regressions of AR counts on the circulation principal components and the Niño 3.4 sea surface temperature (SST) index. From left: the North Atlantic Oscillation (NAO), the growth phase of North Pacific Oscillation/West Pacific (NPO/WP) pattern, the decay phase of NPO/WP, the Pacific North American (PNA) pattern, the Scandinavian (SCAND) pattern, and El Niño. Regressions are shaded red/blue for positive/negative anomalies at 0.2 AR/pentad intervals with the zero-contour suppressed. A 9-point spatial smoother is applied twice to AR regressions.

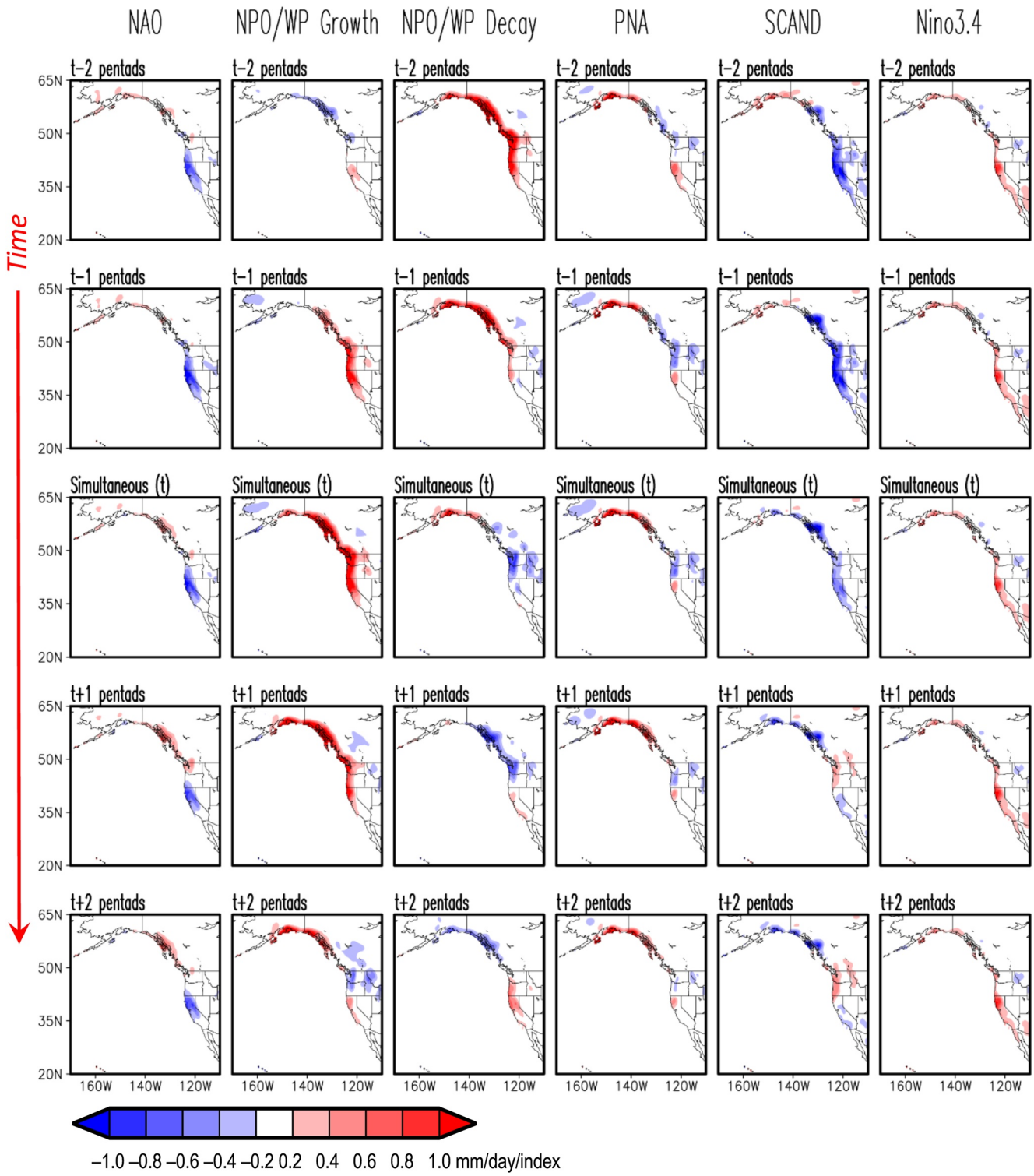

Figure 7. *Pentad* evolution of NOAA precipitation associated with leading subseasonal winter teleconnections and El Niño variability along the North American West Coast. Time runs downward from $t-2$ to $t+2$ pentads. The anomalies are obtained from *pentad* lead-lag linear regressions of precipitation anomalies on the circulation principal components and the Niño 3.4 sea surface temperature (SST) index. From left: the North Atlantic Oscillation (NAO), the growth phase of North Pacific Oscillation/West Pacific (NPO/WP) pattern, the decay phase of NPO/WP, the Pacific North American (PNA) pattern, the Scandinavian (SCAND) pattern, and El Niño. Regressions are shaded red/blue for positive/negative anomalies at 0.2 mm/day intervals with the zero-contour suppressed. A 9-point spatial smoother is applied twice to precipitation regressions.

anomalies along the west coast of the US are isolated positive precipitation anomalies in northern California (fourth column of Figure 7). The regions with the greatest and most robust AR frequency anomalies (from t to $t + 2$), such as northwestern British Columbia and southern Alaska, saw the most coherent positive precipitation anomalies. This is consistent with these areas being subject to moisture fluxes that are orthogonal to elevation gradients—which are responsible for producing heavy precipitation events. Relative to the winter climatology of AR frequency, in the positive phase of the PNA, there is little difference in AR origin (comparing the black contours and color shading in the fourth panel of Figure 3 right).

4. Discussion

The current analysis focuses on the effect of individual winter teleconnection patterns on AR dynamics and landfalling location/frequency along the west coast of North America. While the impacts of established teleconnection patterns on ARs have been documented in previous studies, few studies have looked at the evolution of such impacts on subseasonal time scales. For example, Guan et al. (2013) looked specifically at the teleconnection patterns that influenced the extreme precipitation in the Sierra Nevada during the 2010/2011 winter season (November–March). From a seasonal mean perspective, the study found that the negative phase of the PNA pattern and the negative phase of the AO were responsible for an increase in the frequency of AR events in California, and the frequency was even more extensive when the PNA and AO were simultaneously in their respective negative phases. However, their study did not investigate how the two modes and associated impacts on ARs evolve on subseasonal time scales.

In addition to the focus on subseasonal evolution, another new aspect of the current study is the emphasis on the NPO/WP, a mode that has not been a particular focus in AR studies so far. The relationship between NPO/WP and AR activity on the west coast of the US has only been noted in Brands et al. (2017), Guirguis et al. (2019), and Tan et al. (2020). In Brands et al. (2017), a North Pacific/Aleutian Low index and a West Pacific index were used separately to calculate their contemporaneous influence on AR activity. Their finding is broadly consistent with the results of the current study. Specifically, a positive developing NPO/WP is found to strengthen and expand the influence of the Aleutian Low. The positive PNA's role is similar, except higher heights build over western Canada and the Pacific Northwest, blocking moisture from entering the western US and funneling it toward British Columbia and the Gulf of Alaska, consistent with PNA's influence on AR activity found in Brands et al. (2017) and the current study. In Guirguis et al. (2019), the nine self-organizing maps affecting contemporaneous AR landfalls in California were found to be related to different combinations of canonical circulation patterns, including the WP. As in the current study, they found the regional circulation patterns to be more influential than ENSO in modulating AR impacts in California. In Tan et al. (2020), the occurrence of ARs along the middle coast of western North America (between British Columbia and northern California) was found to be associated with the negative phase of NPO/WP.

The potential role of NPO/WP in modulating AR activity is exemplified by the drought-breaking, exceptionally wet 2022/2023 winter in the western US, especially in California where the number of AR landfalls was about double the climatology. Among the leading nine teleconnection patterns monitored by NOAA CPC, the WP and the PNA were the two modes that were the most notable during this period in terms of magnitude and persistence—the WP was consistently positive during January–March 2023, with the index exceeding two standard deviations in January and February, meanwhile the PNA was consistently negative, with slightly smaller index values than the WP. While the detailed processes contributing to the exceptionally wet 2022/2023 winter in the western US remain to be investigated, the role of NPO/WP highlighted by the current study adds to potential directions for consideration. Formal studies of AR predictability and predictive skills afforded by NPO/WP are needed to help understand its role relative to other better-studied modes related to ARs.

A number of studies have also documented the effects of ENSO on the landfall location and frequency of ARs—although the literature is not conclusive, which could be partly related to complications from ENSO flavors. For example, Weng et al. (2009) suggested that El Niño Modoki events provide a low-level flow that may favor AR landfalls in the southwestern US, whereas canonical El Niño events do not provide such a favorable condition. Bao et al. (2006) found that the ENSO neutral phase is able to transport tropical moisture from the eastern Pacific to the west coast (via extratropical cyclones) much more readily than during the positive, El Niño phase. In addition to ENSO flavors, possible reasons for discrepancies within the literature include differences in data and

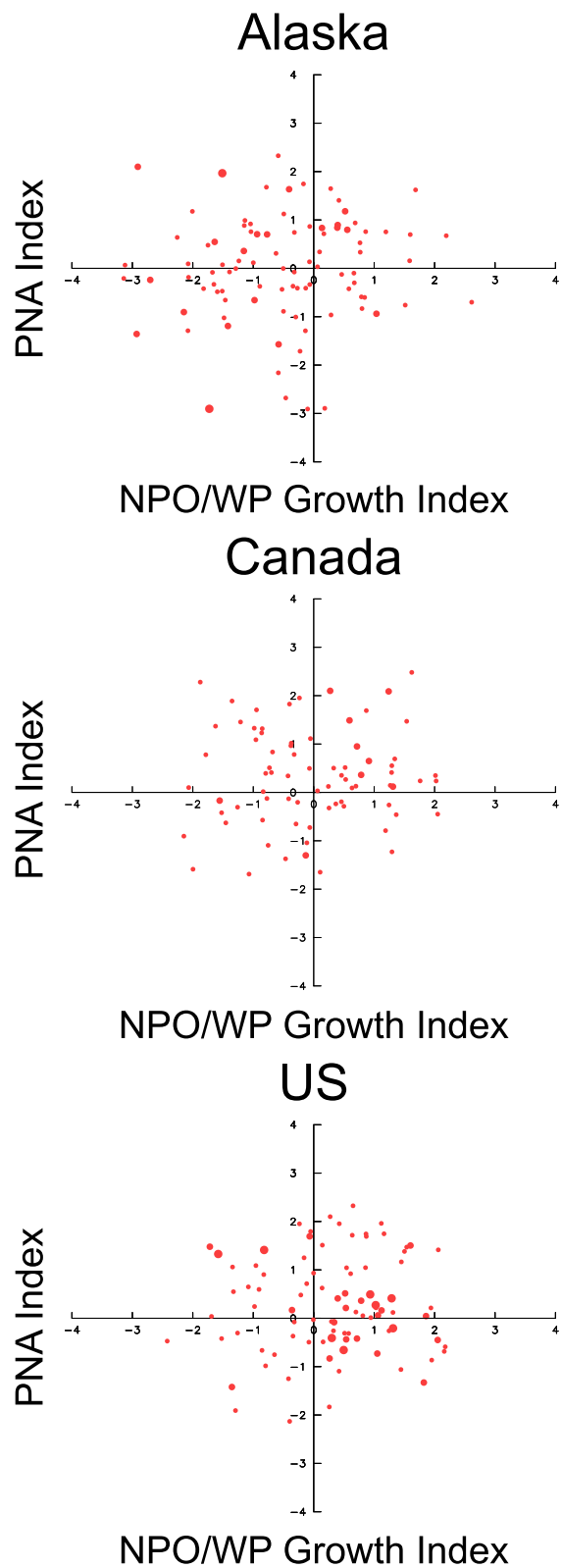

Figure 8. Pentad-count of landfalling atmospheric rivers (ARs) in three coastal regions (the western US, western Canada, and southern Alaska, corresponding to the land portions of the three regions displayed in Figure 6) plotted in the two-dimensional phase space defined by concurrent principal components of the growth phase of North Pacific Oscillation/West Pacific (NPO/WP) pattern and the Pacific North American (PNA) pattern. The dot size represents the region-averaged AR count anomaly; four sizes are plotted, increasing from 3–6, 6–9, 9–12 to >12 ARs/pentad; the negative AR count anomalies are excluded.

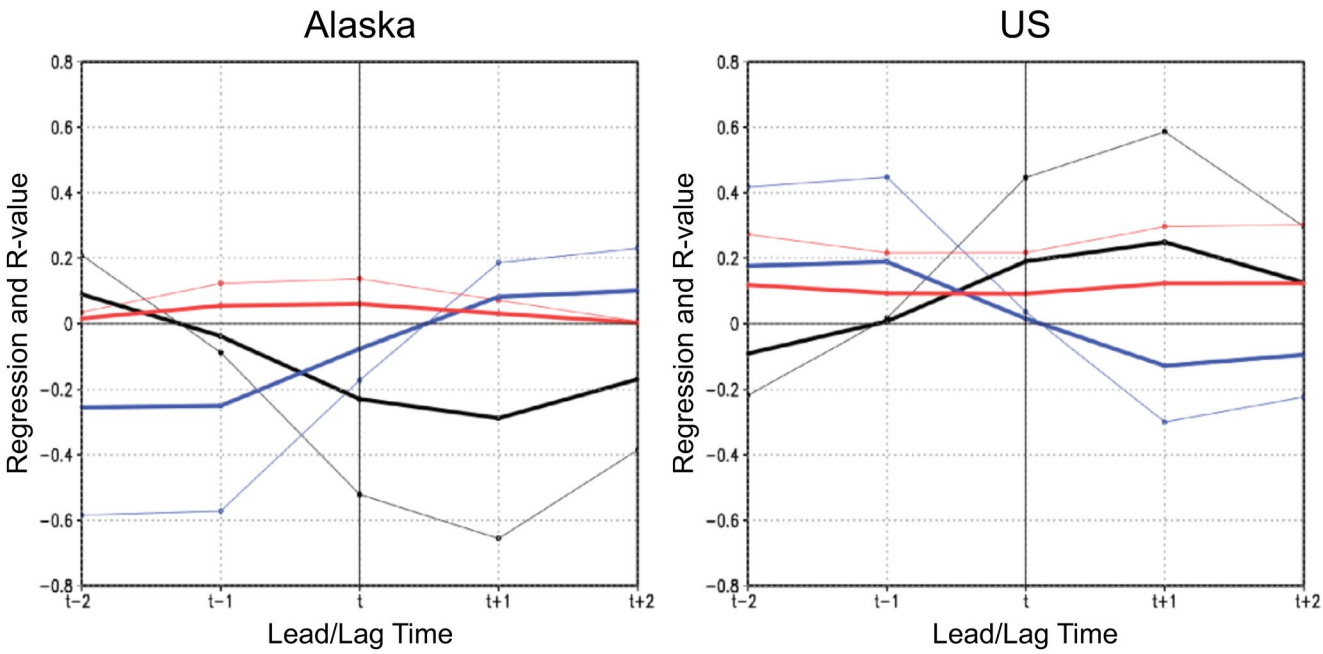

Figure 9. *Pentad* lead-lag regression coefficients and correlations for the landfalling atmospheric rivers (ARs) over southern Alaska (left) and the western US (right) for the growth phase of North Pacific Oscillation/West Pacific (NPO/WP) pattern (black), the decay phase of NPO/WP (blue), and the Pacific North American (PNA) pattern (red). Thin lines represent the regression slopes, while the thick ones the correlation coefficients. The lead-lag analysis is carried out from $t-2$ to $t+2$, with t representing simultaneous values; positive lags indicate principal components leading the ARs. The NPO/WP variability leads to complementary lagged impacts over Alaska and the western US, for example, at $t+1$ and $t+2$ pentads.

methods used to determine the presence of ARs. As a first-order baseline to compare with, the analysis of El Niño influence on ARs in this paper is based on the widely used Niño 3.4 index—which does not distinguish between different ENSO flavors, nor does it separate ENSO-related circulations from other present teleconnections. The relationship between ENSO and ARs will continue to be an ongoing area of study with the lengthening of the observational data record and advancements in methods for more nuanced ENSO characterization (e.g., Williams & Patricola, 2018).

To understand possible interactions between the two most influential teleconnection patterns identified above, the principal components of the two patterns and their influence on AR frequency are further explored for three different landfalling regions (considering grid points over land only): the western US, western Canada, and southern Alaska. A positive NPO/WP growth and a near-neutral PNA were found to coincide with a cluster of large AR frequency anomalies in the western US (Figure 8, bottom panel). No prominent clustering was found to occur in other combinations of the two modes. In western Canada, the PNA pattern is slightly more influential, and a positive PNA and positive NPO/WP growth were found to favor larger AR frequency anomalies than other combinations of the two modes (Figure 8, middle panel). In southern Alaska, the NPO/WP growth pattern appears more influential, with little to no preference of AR frequency anomalies with respect to the PNA phase (Figure 8, top panel). The evolution of these results is shown in Figure 9 and serves to complement the aforementioned figures by displaying the area-averaged regression slopes and correlation coefficients for all three regions. A positive (negative) phase of a growing NPO/WP is the most influential pattern 5 days after its mature phase, that is, at $t+1$, when the regression value is about 0.6 (0.65) and the R-value is about 0.25 (0.30). A positive PNA is slightly more influential in Canada than the growth/decay patterns of the NPO/WP, especially 5 days after the mature phase when the regression value and R-value are about 0.4 and 0.2, respectively.

To corroborates what is shown in the AR and precipitation regressions, moisture flux and its convergence are regressed onto the leading teleconnection patterns. It is found that moisture flux convergence is largest along the west coast of the US from $t-1$ to $t+1$ during the positive NPO/WP growth phase (>1 mm/day per unit index) and moisture fluxes are largest and most orthogonal to the topography in its mature phase (Figure 10, left column). Moisture

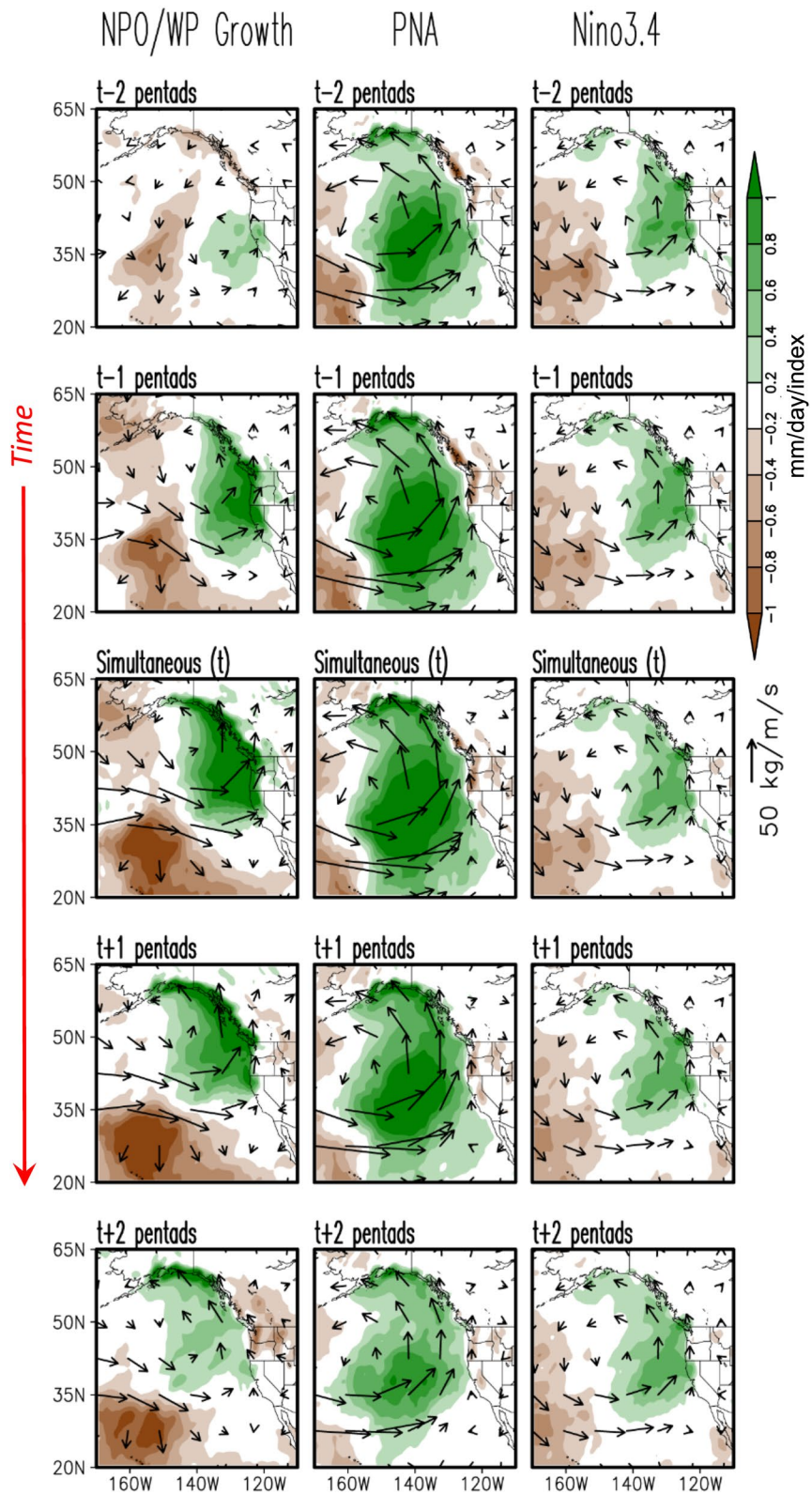

Figure 10.

convergence is concentrated offshore and along coastal Alaska in a positive PNA, and moisture divergence is present throughout most of the coastal Pacific Northwest. The moisture fluxes are parallel to the topography of the western US, resulting in enhanced AR activity poleward into coastal northwestern British Columbia and southern Alaska (Figure 10, middle column). Weaker moisture flux and convergence associated with El Niño are consistent with its less influential modulation of AR frequency along western North America (Figure 10, right column).

5. Conclusion

Previous studies found the PNA to be an influential mode in modulating AR activity along the west coast of North America. In this study, however, the growth phase of NPO/WP emerges as the leading pattern for modulating AR landfalling frequency, especially between the Pacific Northwest and central California as well as southern Alaska. In its positive phase, the presence of anomalous low pressure centered just south of Alaska (i.e., a strengthening of the Aleutian Low) and anomalous high pressure around Hawaii results in moisture convergence in the central and eastern Pacific, bringing southwesterly moisture fluxes to coastal and inland areas. This increases the number of ARs that make landfall on the west coast. Although southwesterly fluxes are stronger over the Pacific Ocean during positive PNA, they tend to transition to southerly fluxes before extending inland. This results in a smaller increase in landfalling ARs during positive PNA than during positive NPO/WP growth.

These results are coupled with lead/lag regression analysis to provide the answer to *when* each pattern exerts the greatest influence on landfalling ARs. Both the NPO/WP (in its positive growth phase) and the PNA modulate coastal ARs especially 5 days after their respective mature phases ($t + 1$), although the latter pattern tends to deflect moisture to northwestern British Columbia rather than the western US. However, precipitation does not always follow the same spatiotemporal relationship as ARs partly due to precipitation from non-AR events, but also because precipitation is directly related to the convergence of IVT, rather than IVT itself which defines ARs (Benton & Estoque, 1954; Mo et al., 2021). The greatest precipitation rate during the positive growth phase of the NPO/WP occurs at its mature stage (t; when precipitation neither leads nor lags the principal component) along the western US coast. A positive PNA has only a weaker, isolated influence on coastal precipitation in the western US; the greatest influence occurs in British Columbia 5 days after the mature stage ($t + 1$), consistent with the AR frequency analysis. The study highlights the influential role of the NPO/WP pattern in modulating AR activity compared to other subseasonal circulation patterns. The temporal evolution of AR frequency and precipitation anomalies associated with NPO/WP suggests a potential source of subseasonal predictability that warrants further investigations.

Figure 10. *Pentad* evolution of vertically-integrated moisture flux and its convergence associated with leading subseasonal winter teleconnections and El Niño variability along the North American West Coast. Time runs downward from $t - 2$ to $t + 2$ pentads. The anomalies are obtained from *pentad* lead-lag linear regressions of moisture flux anomalies on the circulation principal components and the Niño 3.4 sea surface temperature (SST) index. From left: the growth phase of North Pacific Oscillation/West Pacific (NPO/WP) pattern, the Pacific North American (PNA) pattern, and El Niño. Regressions are shaded green/brown for moisture-flux convergence/divergence anomalies at 0.2 mm/day/index intervals with the zero-contour suppressed; see color bar. Moisture-flux vectors are shown using black arrows, with the indicated scale. A 9-point spatial smoother is applied twice to moisture-flux regressions.

Data Availability Statement

The MERRA-2 reanalysis (Gelaro et al., 2017) is provided by NASA via https://gmao.gsfc.nasa.gov/reanalysis/MERRA-2/, NCEP/NCAR reanalysis (Kalnay et al., 1996) by NOAA via https://www.esrl.noaa.gov/psd/data/gridded/data.ncep.reanalysis.html, CPC Unified Gauge-Based Analysis of Daily Precipitation (Xie et al., 2007) by NOAA via https://psl.noaa.gov/data/gridded/data.unified.daily.conus.html, and OI SST (Reynolds et al., 2002) by NOAA via https://psl.noaa.gov/data/gridded/data.noaa.oisst.v2.html. The AR detection code (Guan, 2021) is available via the Global Atmospheric Rivers Dataverse (https://dataverse.ucla.edu/dataverse/ar). The graphics are prepared with GrADS (http://cola.gmu.edu/grads/).

Acknowledgments

We would like to thank Dr. Stephen Baxter of the NOAA Climate Prediction Center for providing us with the updated principal components of the atmospheric teleconnections. JH thanks Dr. Tim Canty for his advice and guidance, as well as Dr. Paul Houser who allowed us to store data and perform computations on his server. BG was supported by NASA Grants 80NSSC20K1344, 80NSSC21K1007, and 80NSSC22K0926, and the California Department of Water Resources. The development of the AR detection code was supported by NASA and the California Department of Water Resources.

References

Bao, J.-W., Michelson, S. A., Neiman, P. J., Ralph, F. M., & Wilczak, J. M. (2006). Interpretation of enhanced integrated water vapor bands associated with extratropical cyclones: Their formation and connection to tropical moisture. *Monthly Weather Review*, *134*(4), 1063–1080. https://doi.org/10.1175/MWR3123.1

Baxter, S., & Nigam, S. (2013). A subseasonal teleconnection analysis: PNA development and its relationship to the NAO. *Journal of Climate*, *26*(18), 6733–6741. https://doi.org/10.1175/JCLI-D-12-00426.1

Baxter, S., & Nigam, S. (2015). Key role of the North Pacific Oscillation–West Pacific pattern in generating the extreme 2013/14 North American winter. *Journal of Climate*, *28*(20), 8109–8117. https://doi.org/10.1175/JCLI-D-14-00726.1

Benton, G. S., & Estoque, M. A. (1954). Water-vapor transfer over the North American continent. *Journal of Meteorology*, *11*(6), 462–477. https://doi.org/10.1175/1520-0469(1954)011<0462:WVTOTN>2.0.CO;2

Björnsson, H., & Venegas, S. A. (1997). *A manual for EOF and SVD analyses of climate data*. CCGCR Rep. 97–1 (p. 52). McGill Univ.

Brands, S., Gutiérrez, J. M., & San-Martín, D. (2017). Twentieth-century atmospheric river activity along the west coasts of Europe and North America: Algorithm formulation, reanalysis uncertainty and links to atmospheric circulation patterns. *Climate Dynamics*, *48*(9–10), 2771–2795. https://doi.org/10.1007/s00382-016-3095-6

Collow, A. B. M., Shields, C. A., Guan, B., Kim, S., Lora, J. M., McClenny, E. E., et al. (2022). An overview of ARTMIP's Tier 2 reanalysis intercomparison: Uncertainty in the detection of atmospheric rivers and their associated precipitation. *Journal of Geophysical Research: Atmospheres*, *127*(8), e2021JD036155. https://doi.org/10.1029/2021JD036155

Corringham, T. W., Ralph, F. M., Gershunov, A., Cayan, D. R., & Talbot, C. A. (2019). Atmospheric rivers drive flood damages in the western United States. *Science Advances*, *5*(12), eaax4631. https://doi.org/10.1126/sciadv.aax4631

Dettinger, M. D. (2004). *Fifty-two years of "pineapple-express" storms across the west coast of North America*. CEC-500-2005-004. U.S. Geological Survey, Scripps Institution of Oceanography for the California Energy Commission, PIER Energy-Related Environmental Research. Retrieved from http://www.energy.ca.gov/2005publications/CEC-500-2005-004/CEC-500-2005-004.PDF

Dettinger, M. D. (2013). Atmospheric rivers as drought busters on the U.S. West Coast. *Journal of Hydrometeorology*, *14*(6), 1721–1732. https://doi.org/10.1175/JHM-D-13-02.1

Dettinger, M. D., Ralph, F. M., Das, T., Neiman, P. J., & Cayan, D. R. (2011). Atmospheric rivers, floods and the water resources of California. *Water*, *3*(2), 445–478. https://doi.org/10.3390/w3020445

Eiras-Barca, J., Ramos, A. M., Algarra, I., Vázquez, M., Dominguez, F., Miguez-Macho, G., et al. (2021). European West Coast atmospheric rivers: A scale to characterize strength and impacts. *Weather and Climate Extremes*, *31*, 100305. https://doi.org/10.1016/j.wace.2021.100305

Eiras-Barca, J., Ramos, A. M., Pinto, J. G., Trigo, R. M., Liberato, M. L. R., & Miguez-Macho, G. (2018). The concurrence of atmospheric rivers and explosive cyclogenesis in the North Atlantic and North Pacific basins. *Earth System Dynamics*, *9*(1), 91–102. https://doi.org/10.5194/esd-9-91-2018

Gelaro, R., McCarty, W., Suárez, M. J., Todling, R., Molod, A., Takacs, L., et al. (2017). The modern-era retrospective analysis for research and applications, Version 2 (MERRA-2). *Journal of Climate*, *30*(14), 5419–5454. https://doi.org/10.1175/JCLI-D-16-0758.1

Guan, B. (2021). [Code] Tracking atmospheric rivers globally as elongated targets (tARget), version 3. *UCLA Dataverse*. https://doi.org/10.25346/S6/B89KXF

Guan, B., Molotch, N. P., Waliser, D. E., Fetzer, E. J., & Neiman, P. J. (2010). Extreme snowfall events linked to atmospheric rivers and surface air temperature via satellite measurements: Extreme snowfall and atmospheric rivers. *Geophysical Research Letters*, *37*(20), n/a. https://doi.org/10.1029/2010GL044696

Guan, B., Molotch, N. P., Waliser, D. E., Fetzer, E. J., & Neiman, P. J. (2013). The 2010/2011 snow season in California's Sierra Nevada: Role of atmospheric rivers and modes of large-scale variability: Atmospheric rivers and modes of large-scale variability. *Water Resources Research*, *49*(10), 6731–6743. https://doi.org/10.1002/wrcr.20537

Guan, B., & Waliser, D. E. (2015). Detection of atmospheric rivers: Evaluation and application of an algorithm for global studies: Detection of atmospheric rivers. *Journal of Geophysical Research: Atmospheres*, *120*(24), 12514–12535. https://doi.org/10.1002/2015JD024257

Guan, B., Waliser, D. E., Molotch, N. P., Fetzer, E. J., & Neiman, P. J. (2012). Does the Madden–Julian Oscillation influence wintertime atmospheric rivers and snowpack in the Sierra Nevada? *Monthly Weather Review*, *140*(2), 325–342. https://doi.org/10.1175/MWR-D-11-00087.1

Guan, B., Waliser, D. E., & Ralph, F. M. (2018). An intercomparison between reanalysis and dropsonde observations of the total water vapor transport in individual atmospheric rivers. *Journal of Hydrometeorology*, *19*(2), 321–337. https://doi.org/10.1175/JHM-D-17-0114.1

Guan, B., Waliser, D. E., & Ralph, F. M. (2023). Global application of the atmospheric river scale. *Journal of Geophysical Research: Atmospheres*, *128*(3), e2022JD037180. https://doi.org/10.1029/2022JD037180

Guirguis, K., Gershunov, A., Shulgina, T., Clemesha, R. E. S., & Ralph, F. M. (2019). Atmospheric rivers impacting Northern California and their modulation by a variable climate. *Climate Dynamics*, *52*(11), 6569–6583. https://doi.org/10.1007/s00382-018-4532-5

Hannachi, A. (2004). *A primer for EOF analysis of climate data* (pp. 1–33). University of Reading. Retrieved from http://www.o3d.org/eas-6490/lectures/EOFs/eofprimer.pdf

Kalnay, E., Kanamitsu, M., Kistler, R., Collins, W., Deaven, D., Gandin, L., et al. (1996). The NCEP/NCAR 40-year reanalysis project. *Bulletin of the American Meteorological Society*, *77*(3), 437–471. https://doi.org/10.1175/1520-0477(1996)077<0437:TNYRP>2.0.CO;2

Kim, H.-M., Zhou, Y., & Alexander, M. A. (2019). Changes in atmospheric rivers and moisture transport over the Northeast Pacific and western North America in response to ENSO diversity. *Climate Dynamics*, *52*(12), 7375–7388. https://doi.org/10.1007/s00382-017-3598-9

Kim, J., Guan, B., Waliser, D. E., Ferraro, R. D., Case, J. L., Iguchi, T., et al. (2018). Winter precipitation characteristics in western US related to atmospheric river landfalls: Observations and model evaluations. *Climate Dynamics*, *50*(1–2), 231–248. https://doi.org/10.1007/s00382-017-3601-5

Kirk, R. E. (1996). Practical significance: A concept whose time has come. *Educational and Psychological Measurement*, *56*(5), 746–759. https://doi.org/10.1177/0013164496056005002

Lakshmi, D. D., Satyanarayana, A. N. V., & Chakraborty, A. (2019). Assessment of heavy precipitation events associated with floods due to strong moisture transport during summer monsoon over India. *Journal of Atmospheric and Solar-Terrestrial Physics*, *189*, 123–140. https://doi.org/10.1016/j.jastp.2019.04.013

Lavers, D. A., & Villarini, G. (2013a). The nexus between atmospheric rivers and extreme precipitation across Europe: ARS and extreme European precipitation. *Geophysical Research Letters*, *40*(12), 3259–3264. https://doi.org/10.1002/grl.50636

Lavers, D. A., & Villarini, G. (2013b). Atmospheric rivers and flooding over the central United States. *Journal of Climate*, *26*(20), 7829–7836. https://doi.org/10.1175/JCLI-D-13-00212.1

Lavers, D. A., Villarini, G., Allan, R. P., Wood, E. F., & Wade, A. J. (2012). The detection of atmospheric rivers in atmospheric reanalyses and their links to British winter floods and the large-scale climatic circulation. *Journal of Geophysical Research*, *117*(D20), D20106. https://doi.org/10.1029/2012JD018027

Lee, S. H., Polvani, L. M., & Guan, B. (2022). Modulation of atmospheric rivers by the Arctic stratospheric polar vortex. *Geophysical Research Letters*, *49*(18), e2022GL100381. https://doi.org/10.1029/2022GL100381

Linkin, M. E., & Nigam, S. (2008). The North Pacific Oscillation–West Pacific teleconnection pattern: Mature-phase structure and winter impacts. *Journal of Climate*, *21*(9), 1979–1997. https://doi.org/10.1175/2007JCLI2048.1

Mo, R. (2022). Prequel to the stories of warm conveyor belts and atmospheric rivers: The moist tongues identified by Rossby and his collaborators in the 1930s. *Bulletin of the American Meteorological Society*, *103*(4), E1019–E1040. https://doi.org/10.1175/BAMS-D-20-0276.1

Mo, R., Brugman, M. M., Milbrandt, J. A., Goosen, J., Geng, Q., Emond, C., et al. (2019). Impacts of hydrometeor drift on orographic precipitation: Two case studies of landfalling atmospheric rivers in British Columbia, Canada. *Weather and Forecasting*, *34*(5), 1211–1237. https://doi.org/10.1175/WAF-D-18-0176.1

Mo, R., Lin, H., & Vitart, F. (2022). An anomalous warm-season trans-Pacific atmospheric river linked to the 2021 western North America heatwave. *Communications Earth & Environment*, *3*(1), 127. https://doi.org/10.1038/s43247-022-00459-w

Mo, R., So, R., Brugman, M. M., Mooney, C., Liu, A. Q., Jakob, M., et al. (2021). Column relative humidity and primary condensation rate as two useful supplements to atmospheric river analysis. *Water Resources Research*, *57*(11), e2021WR029678. https://doi.org/10.1029/2021WR029678

Mundhenk, B. D., Barnes, E. A., & Maloney, E. D. (2016). All-season climatology and variability of atmospheric river frequencies over the North Pacific. *Journal of Climate*, *29*(13), 4885–4903. https://doi.org/10.1175/JCLI-D-15-0655.1

Neiman, P. J., Ralph, F. M., Wick, G. A., Lundquist, J. D., & Dettinger, M. D. (2008). Meteorological characteristics and overland precipitation impacts of atmospheric rivers affecting the west coast of North America based on eight years of SSM/I satellite observations. *Journal of Hydrometeorology*, *9*(1), 22–47. https://doi.org/10.1175/2007JHM855.1

Nigam, S. (2003). Teleconnections. In *Encyclopedia of atmospheric sciences* (pp. 2243–2269). Elsevier. https://doi.org/10.1016/B0-12-227090-8/00400-0

O'Brien, T. A., Wehner, M. F., Payne, A. E., Shields, C. A., Rutz, J. J., Leung, L.-R., et al. (2022). Increases in future AR count and size: Overview of the ARTMIP Tier 2 CMIP5/6 experiment. *Journal of Geophysical Research: Atmospheres*, *127*(6), e2021JD036013. https://doi.org/10.1029/2021JD036013

Prince, H. D., Gibson, P. B., DeFlorio, M. J., Corringham, T. W., Cobb, A., Guan, B., et al. (2021). Genesis locations of the costliest atmospheric rivers impacting the western United States. *Geophysical Research Letters*, *48*(20), e2021GL093947. https://doi.org/10.1029/2021GL093947

Ralph, F. M., Neiman, P. J., Wick, G. A., Gutman, S. I., Dettinger, M. D., Cayan, D. R., & White, A. B. (2006). Flooding on California's Russian River: Role of atmospheric rivers. *Geophysical Research Letters*, *33*(13), L13801. https://doi.org/10.1029/2006GL026689

Ralph, F. M., Rutz, J. J., Cordeira, J. M., Dettinger, M., Anderson, M., Reynolds, D., et al. (2019). A scale to characterize the strength and impacts of atmospheric rivers. *Bulletin of the American Meteorological Society*, *100*(2), 269–289. https://doi.org/10.1175/BAMS-D-18-0023.1

Reynolds, R. W., Rayner, N. A., Smith, T. M., Stokes, D. C., & Wang, W. (2002). An improved in situ and satellite SST analysis for climate. *Journal of Climate*, *15*(13), 1609–1625. https://doi.org/10.1175/1520-0442(2002)015<1609:AIISAS>2.0.CO;2

Rutz, J. J., Shields, C. A., Lora, J. M., Payne, A. E., Guan, B., Ullrich, P., et al. (2019). The atmospheric river tracking method intercomparison project (ARTMIP): Quantifying uncertainties in atmospheric river climatology. *Journal of Geophysical Research: Atmospheres*, *124*(24), 13777–13802. https://doi.org/10.1029/2019JD030936

Rutz, J. J., & Steenburgh, W. J. (2012). Quantifying the role of atmospheric rivers in the interior western United States. *Atmospheric Science Letters*, *13*(4), 257–261. https://doi.org/10.1002/asl.392

Sharma, A. R., & Déry, S. J. (2020). Contribution of atmospheric rivers to annual, seasonal, and extreme precipitation across British Columbia and Southeastern Alaska. *Journal of Geophysical Research: Atmospheres*, *125*(9), e2019JD031823. https://doi.org/10.1029/2019JD031823

Shields, C. A., Payne, A. E., Shearer, E. J., Wehner, M. F., O'Brien, T. A., Rutz, J. J., et al. (2023). Future atmospheric rivers and impacts on precipitation: Overview of the ARTMIP Tier 2 high-resolution global warming experiment. *Geophysical Research Letters*, *50*(6), e2022GL102091. https://doi.org/10.1029/2022GL102091

Shields, C. A., Rutz, J. J., Leung, L.-Y., Ralph, F. M., Wehner, M., Kawzenuk, B., et al. (2018). Atmospheric river tracking method intercomparison project (ARTMIP): Project goals and experimental design. *Geoscientific Model Development*, *11*(6), 2455–2474. https://doi.org/10.5194/gmd-11-2455-2018

Smirnov, V. V., & Moore, G. W. K. (1999). Spatial and temporal structure of atmospheric water vapor transport in the Mackenzie River Basin. *Journal of Climate*, *12*(3), 681–696. https://doi.org/10.1175/1520-0442(1999)012<0681:SATSOA>2.0.CO;2

Tan, Y., Yang, S., Zwiers, F., Wang, Z., & Sun, Q. (2022). Moisture budget analysis of extreme precipitation associated with different types of atmospheric rivers over western North America. *Climate Dynamics*, *58*(3–4), 793–809. https://doi.org/10.1007/s00382-021-05933-3

Tan, Y., Zwiers, F., Yang, S., Li, C., & Deng, K. (2020). The role of circulation and its changes in present and future atmospheric rivers over western North America. *Journal of Climate*, *33*(4), 1261–1281. https://doi.org/10.1175/JCLI-D-19-0134.1

Wang, J., DeFlorio, M. J., Guan, B., & Castellano, C. M. (2023). Seasonality of MJO impacts on precipitation extremes over the western United States. *Journal of Hydrometeorology*, *24*(1), 151–166. https://doi.org/10.1175/JHM-D-22-0089.1

Weare, B. C., & Nasstrom, J. S. (1982). Examples of extended empirical orthogonal function analyses. *Monthly Weather Review*, *110*(6), 481–485. https://doi.org/10.1175/1520-0493(1982)110<0481:EOEEOF>2.0.CO;2

Weng, H., Behera, S. K., & Yamagata, T. (2009). Anomalous winter climate conditions in the Pacific rim during recent El Niño Modoki and El Niño events. *Climate Dynamics*, *32*(5), 663–674. https://doi.org/10.1007/s00382-008-0394-6

Williams, I. N., & Patricola, C. M. (2018). Diversity of ENSO events unified by convective threshold sea surface temperature: A nonlinear ENSO index. *Geophysical Research Letters*, *45*(17), 9236–9244. https://doi.org/10.1029/2018GL079203

Xie, P., Chen, M., Yang, S., Yatagai, A., Hayasaka, T., Fukushima, Y., & Liu, C. (2007). A gauge-based analysis of daily precipitation over East Asia. *Journal of Hydrometeorology*, *8*(3), 607–626. https://doi.org/10.1175/JHM583.1

Yang, Y., Zhao, T., Ni, G., & Sun, T. (2018). Atmospheric rivers over the Bay of Bengal lead to northern Indian extreme rainfall. *International Journal of Climatology*, *38*(2), 1010–1021. https://doi.org/10.1002/joc.5229

Zhang, W., & Villarini, G. (2018). Uncovering the role of the East Asian jet stream and heterogeneities in atmospheric rivers affecting the western United States. *Proceedings of the National Academy of Sciences*, *115*(5), 891–896. https://doi.org/10.1073/pnas.1717883115

Zhou, Y., Kim, H., & Waliser, D. E. (2021). Atmospheric river lifecycle responses to the Madden-Julian Oscillation. *Geophysical Research Letters*, *48*(3), e2020GL090983. https://doi.org/10.1029/2020GL090983

Zhu, Y., & Newell, R. E. (1994). Atmospheric rivers and bombs. *Geophysical Research Letters*, *21*(18), 1999–2002. https://doi.org/10.1029/94GL01710

Zhu, Y., & Newell, R. E. (1998). A proposed algorithm for moisture fluxes from atmospheric rivers. *Monthly Weather Review*, *126*(3), 725–735. https://doi.org/10.1175/1520-0493(1998)126<0725:APAFMF>2.0.CO;2